

A Single Atom Change Turns Insulating Saturated Wires into Molecular Conductors

Xiaoping Chen

National University of Singapore

Bernhard Kretz

Technical University of Munich

Francis Adoah

University of Central Florida

Cameron Nickle

University of Central Florida

Xiao Chi

National University of Singapore

Xiao-Jiang Yu

National University of Singapore <https://orcid.org/0000-0002-7044-6417>

Enrique del Barco

University of Central Florida <https://orcid.org/0000-0002-5763-0076>

Damien Thompson

University of Limerick <https://orcid.org/0000-0003-2340-5441>

David Egger

University of Regensburg

christian nijhuis (✉ chmnca@nus.edu.sg)

National University of Singapore <https://orcid.org/0000-0003-3435-4600>

Article

Keywords: tunnelling methods, terminal-atom substitution, new charge transport models, molecular tunnelling junctions

Posted Date: September 9th, 2020

DOI: <https://doi.org/10.21203/rs.3.rs-69097/v1>

License:   This work is licensed under a Creative Commons Attribution 4.0 International License.

[Read Full License](#)

Version of Record: A version of this preprint was published at Nature Communications on June 8th, 2021.
See the published version at <https://doi.org/10.1038/s41467-021-23528-8>.

A Single Atom Change Turns Insulating Saturated Wires into Molecular Conductors

Xiaoping Chen^{1,2}, Bernhard Kretz³, Francis Adoah⁴, Cameron Nickle⁴, Xiao Chi⁵, Xiaojiang Yu⁵, Enrique del Barco⁴, Damien Thompson⁶, David A. Egger^{3}, and Christian A. Nijhuis^{1,2*}*

¹Department of Chemistry, National University of Singapore, 3 Science Drive 3, Singapore 117543, Singapore.

²Centre for Advanced 2D Materials and Graphene Research Centre, National University of Singapore, 6 Science Drive 2, Singapore 117546, Singapore.

³Department of Physics, Technical University of Munich, 85748 Garching, Germany

⁴Department of Physics, University of Central Florida, Orlando, Florida 32816 - USA

⁵Singapore Synchrotron Light Source, National University of Singapore, 5 Research Link, Singapore 117603, Singapore.

⁶Department of Physics, Bernal Institute, University of Limerick, V94 T9PX, Ireland

*Correspondence to: chmnca@nus.edu.sg; david.egger@tum.de

Abstract:

We present an efficient strategy to modulate tunnelling in molecular junctions by changing the tunnelling decay coefficient, β , by terminal-atom substitution which avoids altering the molecular backbone. By varying X=H, F, Cl, Br, I in junctions with $S(CH_2)_{(10-18)}X$, current densities (J) increases >4 orders of magnitude, creating molecular conductors *via* reduction of β from 0.75 to 0.25\AA^{-1} . Impedance measurements shows tripled dielectric constants (ϵ_r) with X=I, reduced HOMO-LUMO gaps and tunnelling-barrier heights, and 5-times reduced contact resistance. These effects alone cannot explain the large change in β . Density-functional theory shows highly localized, X-dependent potential drop at the $S(CH_2)_nX$ //electrode interface that modifies the tunnelling barrier shape. Commonly-used tunnelling models neglect localized potential drops and changes in ϵ_r . We demonstrate experimentally that $\beta \propto 1/\sqrt{\epsilon_r}$, suggesting highly-polarizable terminal-atom sites act as charge traps as proposed by Berlin and Ratner. Our work shows the need for new charge transport models that account for dielectric effects in molecular tunnelling junctions.

Introduction

Significant effort has been dedicated to study and manipulate tunnelling rates across molecular wires, which serve as model systems to improve our understanding of the mechanisms of charge transport across molecules which, in turn, play a central role in, *e.g.*, biological processes, catalysis, and energy conversion.^{1, 2, 3, 4} It is well-known that the tunnelling current density (J in A/cm^2) decreases exponentially with the length of the molecular wire (d in \AA) given by the general tunnelling equation

$$J = J_0(V)e^{-\beta d} = J_0(V)10^{-\beta d/2.303}, \quad (1)$$

where J_0 is a pre-exponential factor and the tunnelling decay coefficient (β in \AA^{-1}) determines how quickly the measured current decays with d .^{2, 5, 6, 7} In this context, unsaturated molecules with conjugated π -bonds are usually thought of as “molecular conductors” with low values of

β ($0.1-0.4 \text{ \AA}^{-1}$)^{2, 5, 8, 9, 10} and saturated molecular wires with localized σ -bonds provide “molecular insulators” with large values of β ($0.8-1.2 \text{ \AA}^{-1}$)^{2, 5, 7, 11, 12, 13}. This rule of thumb stands in sharp contrast with the high tunnelling rates established for various biomolecules,^{14, 15} molecular wires of oligo-peptides,^{16, 17} and oligosilanes¹⁸. These all have saturated molecular backbones yet they exhibit low values of β ($0.1-0.5 \text{ \AA}^{-1}$), and support long-range tunnelling over remarkably large distances of up to tens of nanometres^{15, 19, 20}.

Here, we show that the value of β of molecular wires with an alkyl chain backbone can be reduced from 0.75 \AA^{-1} to 0.25 \AA^{-1} , in effect turning them from insulators into conductors, by introducing one distal polarizable atom at one end of the molecular wire of the form $\text{HS}(\text{CH}_2)_n\text{X}$, with $\text{X} = \text{H, F, Cl, Br, or I}$, with $n = 10-18$ (only even values of n). To the best of our knowledge, this is the first example of tuning β across alkyl chains opening up new ways to control tunnelling rates in junctions. On the basis of experimental and theoretical data, we discuss how introducing this polarizable atom changes the electrostatic potential profile of the tunnelling barrier, the static dielectric constant (ϵ_r) of the junction, and the contact resistance, which are important to consider when modifying tunnelling efficiency across molecular wires.

So far, it has been challenging to engineer β in experiments, and this difficulty is also reflected in various established mechanisms of charge transport across molecular wires. Often, coherent tunnelling is assumed (Eq. 1), where β can be related to the tunnelling barrier height δE_{ME} (defined by the offset in energy between the energy of the Fermi level, E_F , of the electrode and the energy of the molecular frontier orbital relevant for charge transport), as $\beta \propto \sqrt{\delta E_{ME}}$.^{2, 5, 21} This explains why conjugated molecules, which often have frontier orbitals aligned close to E_F , have lower values of β than saturated molecules, which have frontier orbitals further from E_F . Conversely, in the McConnell superexchange model, charge carriers tunnel *via* virtual states defined by the repeat units of the molecular wire; here, the tunnelling rate depends on the interaction strength between the repeat units of the molecular bridge.^{2, 5, 22,}

^{23, 24} This model has been used to explain low β values (0.2-0.5 \AA^{-1}) measured across tunnel junctions with self-assembled monolayers (SAMs) that have σ -bond backbones of oligoglycines,¹⁶ oligoprolines,²⁵ and oligoglycols¹⁷. Furthermore, for very long molecules (*e.g.*, proteins), a flickering resonance model has been proposed to explain long-range tunnelling and low β values.^{15, 26, 27} Finally, different types of hopping models have been proposed to explain low β values of, for instance, bacterial nanowires,²⁶ DNA,²⁸ proteins,²⁹ and long conjugated molecular wires^{18, 30, 31, 32}; here the value of β also depends on the coupling strength between the repeat units, but these models predict a thermally activated component^{10, 30, 31, 32}. To summarize, all previous models suggest the necessity of tuning the chemical nature of the molecular wire in order to change the value of β .

We note that the value of β also depends, besides the chemical nature of the molecular backbone,^{2, 5, 15, 16, 17} on the molecule–electrode coupling strength Γ that is naturally related to δE_{ME} ^{31, 33, 34}. For molecular wires, where δE_{ME} decreases with the number of repeat units due to an increase in conjugation with increasing molecular length, extremely low ($<0.1 \text{\AA}^{-1}$)^{30, 31, 35, 36} and even negative β values have been reported^{35, 37, 38, 39, 40}. Such low β values are also a signature of incoherent hopping and these junctions, in particular those containing redox centres, may operate in this hopping regime (also called incoherent tunnelling regime).^{30, 31, 37}

So far, the influence of electrostatic effects in molecular tunnelling junctions on β has been largely ignored. One way of quantifying trends in the electrostatics of various systems is by studying the ϵ_r of molecular junctions, a macroscopic observable that can be measured *via* impedance spectroscopy.⁴¹ Previous work focused mainly on π -conjugated systems and established that in densely-packed SAMs, ϵ_r hardly changes when the polarizability of the molecules of a SAM, α , is tuned due to depolarization effects (*e.g.*, induced dipoles in neighbouring molecules).^{42, 43, 44} However, it is not known how α affects the tunnelling behaviour of junctions in which depolarization effects are reduced to a minimum. In addition,

the molecular ionization potential (IP) directly relates to α and, consequently, changing α affects molecular frontier orbital energies^{45, 46} and the energy level alignment of molecule–electrode interfaces^{47, 48}, but it is disputed whether an increase in α changes the conductance of the junction^{46, 47, 48, 49}. Also not currently understood is how α affects the relationship between ϵ_r and β . In principle, polarizable groups screen applied electric fields⁵⁰ or result in an induced dipole and, therefore, also affect the potential drop profile inside junctions^{46, 47, 51}. Thus, polarizable atoms or moieties are expected to have a large effect on the measured tunnelling rates, but so far experimental examples are rare and conflicting.^{46, 47, 49, 51} Here, we show that by introducing a single polarizable atom per molecule inside the junctions, the value of β can be reduced by a factor of 3 without changing the chemical structure of the backbone of the molecular wire. In terms of absolute values of J along long molecular wires of $S(\text{CH}_2)_{18}\text{X}$, the value of J increases by a factor of $10^{4.5}$ when X is changed from H to I. Our results demonstrate how an increasing polarizability of X changes the energy level alignment, the molecule–electrode coupling, and ϵ_r . These findings may stimulate new strategies for optimizing tunnelling rates across junctions.

Results and Discussions

The Junctions. Figure 1 shows a schematic illustration of the $\text{Ag-S}(\text{CH}_2)_n\text{X//GaO}_x/\text{EGaIn}$ junctions with $n = 10, 12, 14, 16, \text{ or } 18$, and $\text{X} = \text{H, F, Cl, Br, or I}$, and indicates how the coupling and energy level alignment (*i.e.*, Γ and δE_{ME}) change with X as discussed in detail below. The schematic also includes the equivalent circuit consisting of the contact resistance (R_C , in $\text{m}\Omega\cdot\text{cm}^2$) in series with a parallel combination of the SAM resistance (R_{SAM} , in $\Omega\cdot\text{cm}^2$) and the capacitance of the SAM (C_{SAM} , in $\mu\text{F}/\text{cm}^2$) in the junction. It highlights that the junctions are essentially parallel plate capacitors in which dielectric behaviour depends on the chemical structure of the junctions, which, as we show below, is also important to explain

tunnelling rates. All SAM precursors were synthesized following previously reported methods and characterised with ^1H NMR, ^{13}C NMR, and mass spectroscopy (Sections S1-2). The SAMs were formed on template-stripped Ag electrodes using well-established methods and the junctions were completed with cone-shaped $\text{GaO}_x/\text{EGaIn}$ top contacts⁵² (Sections S3 and S6). Previously, we have reported that for EGaIn junctions with $\text{S}(\text{CH}_2)_n\text{X}$ SAMs (there only $n = 11$ was studied) the measured current increased by 3 orders of magnitude and the value of ϵ_r increased by a factor of 4, when X was changed along the halogen series from F to I⁴⁶. Here we address whether this increase in current is caused by changes in R_C or changes inherent to the tunnelling process (*i.e.*, β). Changing the value of n for each X allows us to investigate in detail how and why β changes as a function of X while keeping the nature of the molecule-electrode interfaces and the molecular backbone the same.

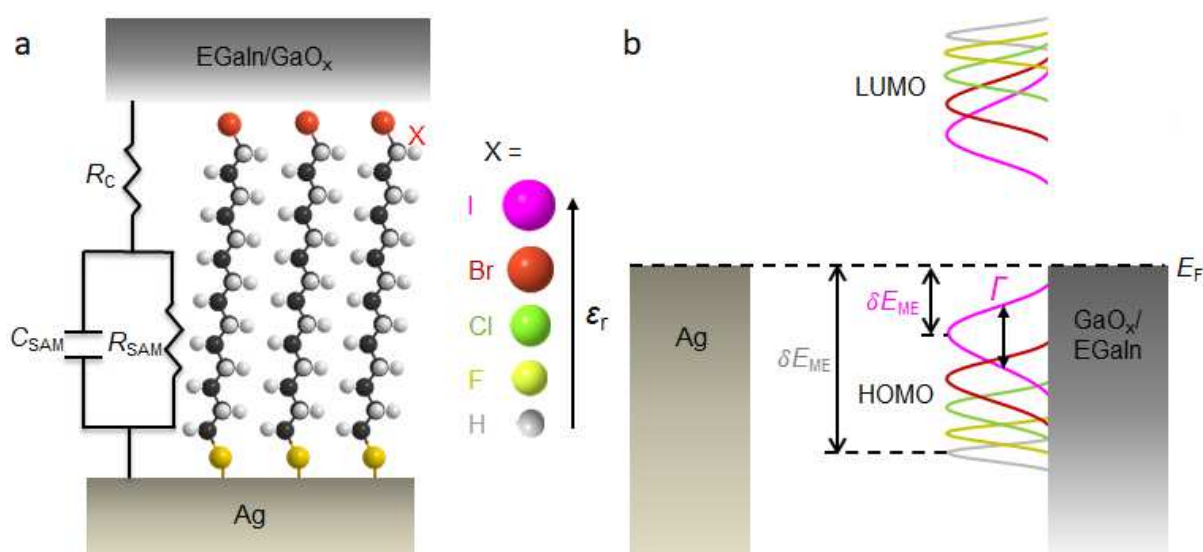


Figure 1. (a) Schematic illustration of the $\text{Ag-S}(\text{CH}_2)_n\text{X}/\text{GaO}_x/\text{EGaIn}$ junction (shown for $n = 14$) together with the equivalent circuit diagram. In this work we investigated junctions with $n = 10, 12, 14, 16,$ or $18,$ and $\text{X} = \text{H}, \text{F}, \text{Cl}, \text{Br},$ or $\text{I}.$ (b) Energy level diagram of the junction showing how Γ and δE_{ME} change with X.

Characterisation of the SAMs. We characterised the SAMs on Ag with $n = 14$ for $X = \text{H}, \text{F}, \text{Cl}, \text{Br}, \text{or I}$, and $n = 10, 14, \text{ or } 18$ for $X = \text{Br}$ with angle resolved X-ray photoelectron spectroscopy (ARXPS) and molecular dynamics (MD) simulations (for all combinations of n and X) and all results are summarized in Table 1 (see Sections S4-5 for details). Figure 2a shows a representative snapshot from the MD simulations of Ag-S(CH₂)₁₄I SAM with computed molecule heights in excellent agreement with film thicknesses d_{SAM} measured by XPS (Figs. 2b-c, Table 1) indicating that the S(CH₂)₁₄I precursor readily forms dense layers with all molecules in a fully-upright position. We determined the relative values of surface coverage (Ψ_{SAM}) with XPS which confirms that all SAMs have indistinguishable packing densities (Figs. 2b-c) within experimental error. The value of $d_{\text{SAM,MD}}$ increases by about 1.4 Å overall on increasing van der Waals radius of X from H to I (Table S1), but this small increase falls within the experimental error of $d_{\text{SAM,XPS}}$ (Fig. 2b). Figure 2c shows that for $X = \text{Br}$, $d_{\text{SAM,XPS}}$ increases linearly with n with a slope of 1.5 ± 0.1 Å per carbon (solid blue line, error represents standard error from linear fit), which is in close agreement with the MD value of 1.3 ± 0.1 Å per carbon (dashed blue line; see Fig. S11 for $d_{\text{SAM,MD}}$ values of all the SAMs). Figure 2d shows the packing energies per molecule ($E_{\text{mol,MD}}$, in eV) and per methylene CH₂ unit ($E_{\text{meth,MD}}$, in meV) extracted from the MD calculations. The values of $E_{\text{mol,MD}}$ and $E_{\text{meth,MD}}$ improve slightly as X shifts from H (-1.8 ± 0.1 eV per molecule) to Br (-2.4 ± 0.2 eV per molecule), which is due to the increasing intermolecular van der Waals interaction. For SAMs with $X = \text{I}$, the packing energies weaken slightly due to small competing effects caused by mild steric repulsion between the large I headgroups. These observations confirm that the halogen functionality does not significantly disrupt the supramolecular structure of the SAM. Finally, we determined the energy level alignment of the SAMs on Ag using ultra-violet photoemission spectroscopy (UPS) in Section S4 and Fig. S10, which we used to validate our DFT calculations as discussed in more detail below (Table 1).

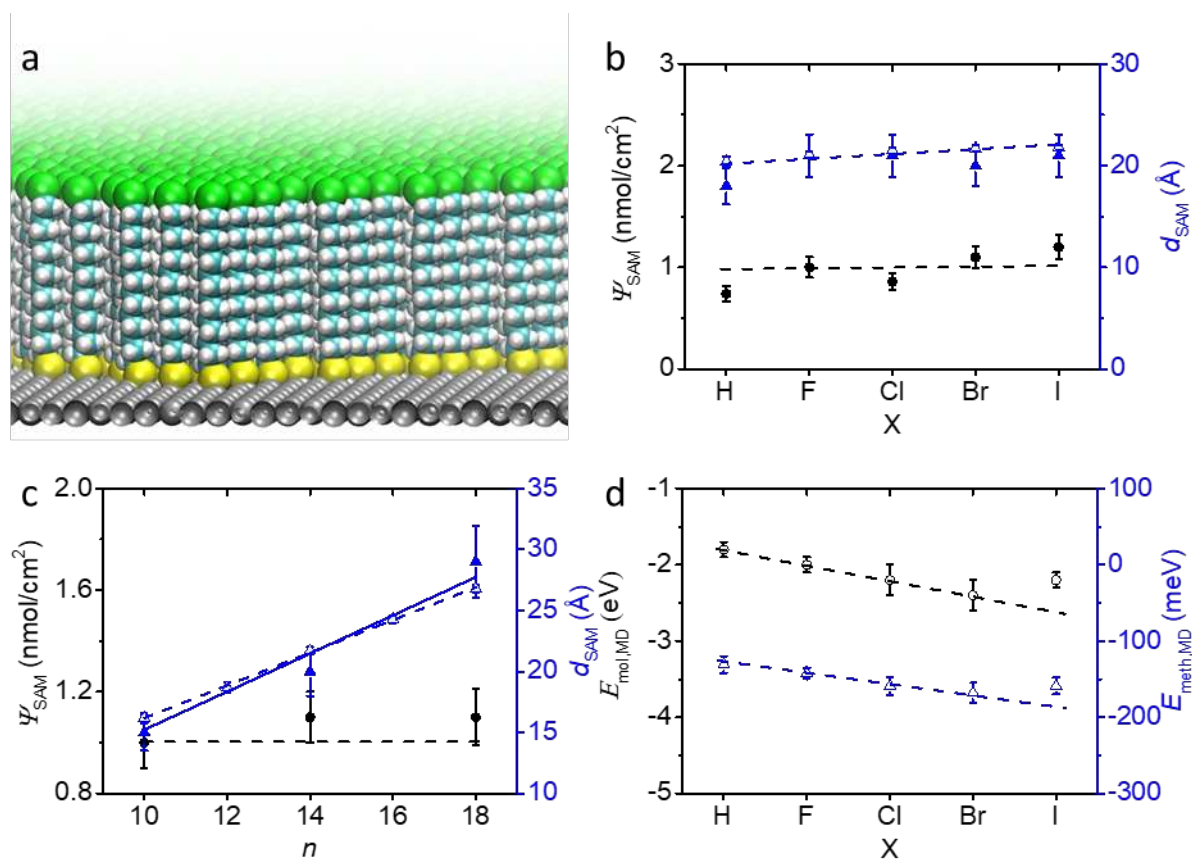


Figure 2. (a) Representative slice-through of a large-area Ag-S(CH₂)₁₄I SAM structure calculated by MD computer simulations. (b) Ψ_{SAM} of Ag-S(CH₂)₁₄X SAMs as a function of X determined with ARXPS (filled circles) and d_{SAM} determined with ARXPS (filled triangles) and MD (empty triangles). (c) Ψ_{SAM} of Ag-S(CH₂)_nBr SAMs as a function of n determined with ARXPS (filled circles) and d_{SAM} determined with ARXPS (filled triangles) and MD (open triangles). The solid and dashed blue lines are linear fits to the experimental and MD data with R^2 of 0.94 and 0.99, respectively. The horizontal dashed line in panels b and c indicates the Ψ_{SAM} used in the MD calculations. (d) Computed MD packing energy per molecule $E_{\text{mol,MD}}$ and per methylene -CH₂- unit $E_{\text{meth,MD}}$ of Ag-S(CH₂)₁₄X SAMs as a function of X. Dashed lines are guides to the eye. The errors on the XPS data represent instrumental and fitting errors of 10% in total (see Section S4). The error bars in the MD data represent the standard deviations in the time- and molecule-averages calculated across 500 snapshots taken during the final 50

ns of 100 ns of room temperature MD of 128-molecule Ag-S(CH₂)₁₄X SAMs with the average experimental coverage of 1 nmol/cm² on Ag(111).

Table 1. Summary of properties of the Ag-S(CH₂)₁₄X and Ag-S(CH₂)_{*n*}Br SAMs

X and <i>n</i>	$\Psi_{\text{SAM,XPS}}$ (nmol/cm ²) ^a	$d_{\text{SAM,XPS}}$ (Å)	$d_{\text{SAM,MD}}$ (Å)	$E_{\text{mol,MD}}$ (eV)	Φ_{SECO} (eV) ^b	Φ_{DFT} (eV)	β (Å ⁻¹)	ϵ_r	$\epsilon_{\text{DFT-vdW}}$
<i>n</i> = 14, X = H	0.74	18	20.4±0.5	-1.8±0.1	3.46	3.76	0.75±0.04	2.9±0.3	2.2
<i>n</i> = 14, X = F	1.0	21	21.1±0.3	-2.0±0.1	4.42	5.05	0.70±0.02	2.5±0.6	2.2
<i>n</i> = 14, X = Cl	0.86	21	21.5±0.3	-2.2±0.2	4.45	5.33	0.60±0.03	3.0±0.2	2.3
<i>n</i> = 14, X = Br	1.1	20	21.7±0.3	-2.4±0.2	4.34	5.36	0.39±0.04	4.7±0.9	2.3
<i>n</i> = 14, X = I	1.2	21	21.8±0.3	-2.2±0.1	4.05	5.26	0.25±0.01	8.9±1.6	2.4
<i>n</i> = 10, X = Br	1.0	15	16.2±0.4	-1.7±0.1	4.28	-	-	4.4±0.4	-
<i>n</i> = 18, X = Br	1.1	29	26.8±0.3	-3.0±0.2	3.96	-	-	4.6±0.2	-

^a The $\Psi_{\text{SAM,XPS}}$ are relative to Ψ_{SAM} of Ag-S(CH₂)₁₄F SAM as measured by XPS.

^b The experimental error is ±0.05 eV.

Electrical characterisation of the junctions. To study how the halogen functionality affects the tunnelling rates across the SAMs, we measured the electrical characteristics of the junctions as a function of X and *n* using $J(V)$ measurements and impedance spectroscopy. The SAMs were contacted with cone-shaped GaO_x/EGaIn electrodes following a previously reported method.⁵² To minimize leakage currents and to ensure that molecular effects dominate the junction characteristics, we used junctions with a small contact area of ~350 μm², as large junctions suffer from leakage currents across defective sites.⁵³ We recorded statistically large numbers of $J(V)$ curves to determine the Gaussian log-average $J(V)$ curves, $\langle \log_{10}|J| \rangle_G$, and associated Gaussian log-standard deviations ($\sigma_{\log,G}$) which are plotted in Fig. 3a for junctions with X = F, and in Fig. 3b for junctions with X = I, for *n* = 10-18 (all Gaussian log-average $J(V)$ curves and histograms of the $\log_{10}|J|$ at ±0.5 V are given in Section S6). Clearly, the tunnelling rates are more attenuated for X = F than for X = I. Figure 3c shows the decay of $\langle \log_{10}|J| \rangle_G$ at -0.5 V as a function of $d_{\text{SAM,MD}}$ (Section S5, Table S1) for all X. The solid lines are fits to Eq. 1 from which we determined the values of β which are listed in Table 1. Interestingly, the value of β steadily decreases from $0.75 \pm 0.01 \text{ \AA}^{-1}$ for X = H – a typical value for tunnelling along alkyl chains – to $0.25 \pm 0.01 \text{ \AA}^{-1}$ for X = I which is a typical value for

tunnelling along π -conjugated molecules (the error in β represents the standard error of the fit to Eq. 1). We measured the $J(V)$ characteristics as a function of temperature, T in K, of Ag-S(CH₂)₁₄X//GaO_x/EGaIn junctions for all X. Figure 3d shows that the tunnelling rates are independent of T in the range of T from 250 to 340 K which is consistent with coherent off-resonant tunneling.⁵⁴

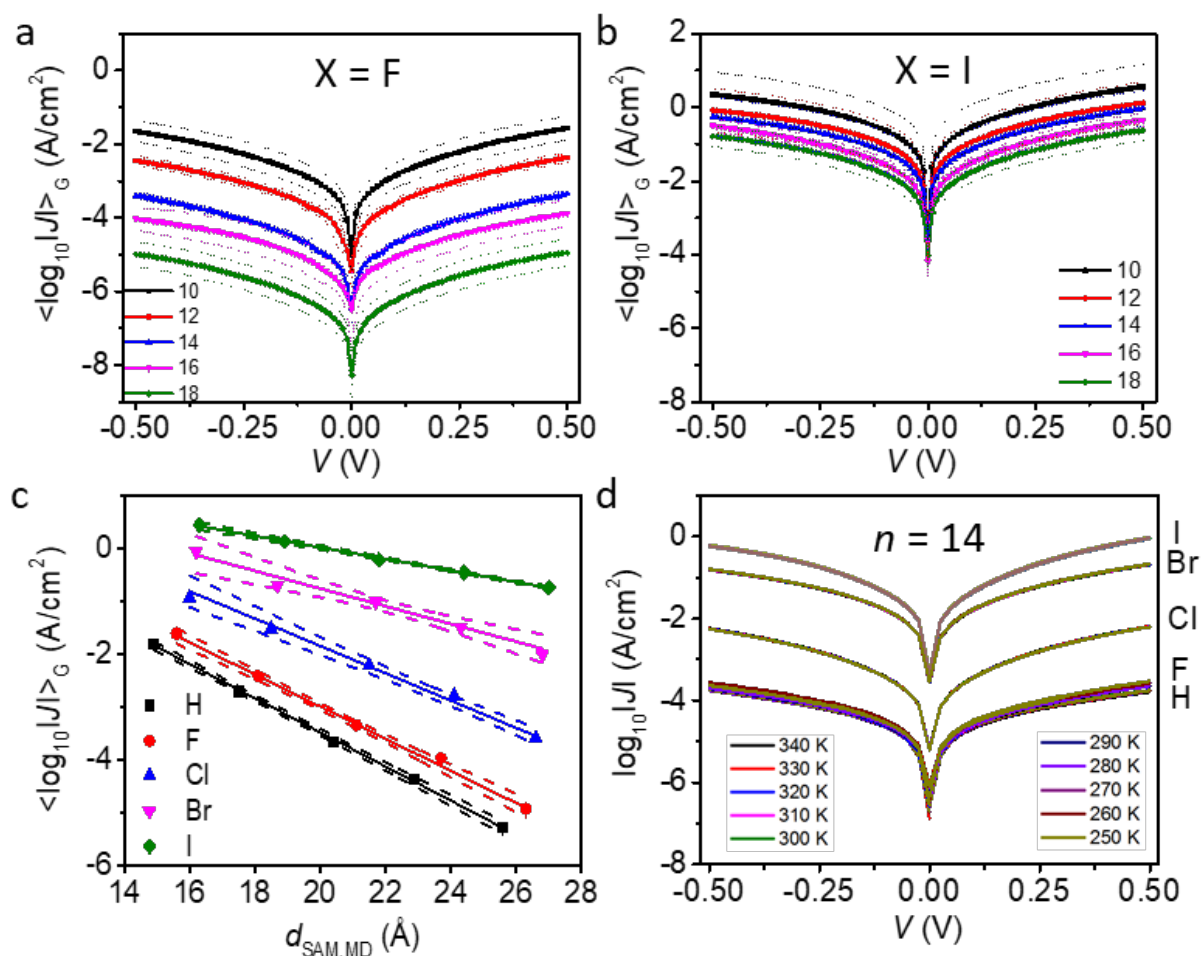


Figure 3. $\langle \log_{10}|J| \rangle_G$ vs. V obtained from Ag-S(CH₂)_nX//GaO_x/EGaIn junctions with $X = F$ (a) or I (b) and $n = 10$ (solid black line), 12 (solid red line), 14 (solid blue line), 16 (solid pink line), and 18 (solid green line). The dashed-line error bars represent the Gaussian log-standard deviation, $\sigma_{\log,G}$. (c) Decay plots of $\langle \log_{10}|J| \rangle_G$ at -0.5 V against $d_{\text{SAM,MD}}$ with $X = H$ (black square), F (red circle), Cl (blue triangle), Br (pink inverted triangle), or I (green diamond). The solid lines are fits to Eq. 1. The dashed lines represent the 95% confidence bands. (d) Plots of

$\log_{10}|J|$ vs. V as a function of T ($T = 250 - 340$ K) recorded from Ag-S(CH₂)₁₄X//GaO_x/EGaIn junctions.

Dielectric constant of the junctions. To characterise the dielectric response of the junctions, we conducted impedance spectroscopy using a sinusoidal voltage perturbation with an amplitude of 30 mV around 0 V in the frequency range of 100 Hz to 1.00 MHz and the data were fitted to the equivalent circuit shown in Fig. 1a following a previously reported method⁴¹ (See Section S7 for details). Figs. S21 shows the Bode, Nyquist, and the corresponding phase angle (ζ) vs. frequency (f) plots along with the fits to the equivalent circuit (Tables S7-9 list all fitting results). Figure 4a shows that R_C decreases by a factor of 5 when X is changed from H or F to I while R_C is independent of n (inset to Fig. 4b). This change in R_C is substantially larger than the odd-even effect in R_C which results in a 2.5 m Ω /cm² modulation of R_C in S(CH₂) _{$n-1$} CH₃ SAMs⁵⁵ and indicates that Γ substantially increases as function of X. This increase in Γ can be rationalized by the increase in polarizability α and associated induced dipoles as a function of X resulting in an increase in the van der Waals interaction strength between the SAM and the top contact.⁴⁶

To confirm the consistency between the $J(V)$ and impedance measurements, we determined the value of β from the impedance measurements for junctions with X = Br. The value of R_{SAM} increases exponentially with n (Eq. 2)

$$R_{SAM} = R_{SAM,0}(V)e^{\beta d_{SAM,MD}} = R_{SAM,0}(V)10^{\beta d_{SAM,MD}/2.303} \quad (2)$$

where $R_{SAM,0}$ is a pre-exponential factor. Figure 4b shows the plot of $\log_{10}R_{SAM}$ vs. n along with a fit to Eq. 2 from which we extracted the values of $\beta = 0.41 \pm 0.03$ Å⁻¹ and $\log|J_0| = 2.0 \pm 0.2$ A/cm² which are, within error, the same as those values determined with the $J(V)$ measurements (Fig. 3c and Table 1).

To gain further insight into the dielectric properties of the junctions, we use the parallel plate capacitor equation (Eq. 3) to determine ϵ_r as a function of X and n

$$C_{\text{SAM}} = \epsilon_0 \epsilon_r \frac{A_{\text{geo}}}{d_{\text{SAM,MD}}} \quad (3)$$

wherein ϵ_0 is the vacuum permittivity and A_{geo} is the geometrical area of the junction. Figure 4c shows that ϵ_r increases by a factor of 3 by changing X from H or F to I, yet ϵ_r is independent of n (Tables S8-9). Although this factor 3 increase in ϵ_r is expected for bulk systems which can be described *via* the Clausius-Mosotti relation,⁵⁶ this observation cannot be explained as an intrinsic electrostatic property of the molecular wires, as we will show and discuss below.

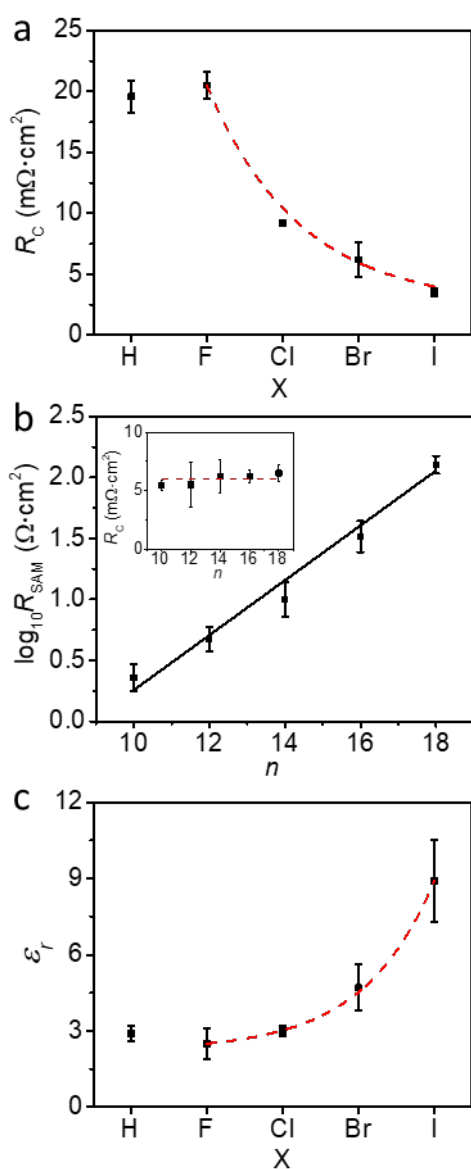


Figure 4. (a) R_C vs. X for Ag-S(CH₂)₁₄X//GaO_x/EGaIn junctions at 0 V. (b) $\log_{10}R_{SAM}$ and R_C (inset) vs. n for Ag-S(CH₂) _{n} Br//GaO_x/EGaIn junctions at 0 V. The solid black line represents a fit to Eq. 2. (c) ϵ_r vs. X for Ag-S(CH₂)₁₄X//GaO_x/EGaIn junctions at 0 V. The error bars are the standard deviations of three independent measurements. Dashed lines are visual guides.

Density functional theory calculations. To provide further microscopic insight into the electrostatic properties and electronic structure of the molecular wires, we performed first-principles calculations based on DFT using the VASP code⁵⁷ (see Section S8 for full details). For Ag-S(CH₂)₁₄X, we find significantly different tilting angles with respect to the surface normal, which span the range of 14.7° (X=H) to 32.8° (X=Cl). Note that these calculated interface geometries are the result of a 0 K optimization of a single-molecule unit cell.

Fig. 5a shows that the shape of the potential energy towards the tail of the alkyl chain strongly depends on the functionalization at the X site. Specifically, the vacuum level changes with X functionalization owing to the polarity of the C-X bond, which translates into a change of the Ag work function, Φ , as expected for SAMs with different tail groups.^{46, 47, 58, 59, 60} Comparing the DFT-calculated Φ to the experimental Φ , it can be seen that the agreement for X=H is excellent (Fig. 5b), while both the absolute values and to a lesser degree also the chemical trends agree not as favourably for the halogen-substituted systems. We tentatively ascribe these deviations to the often observed overestimation of polar effects in periodic DFT calculations of metal-SAM interfaces due to the assumption of perfect molecular order and periodicity,⁶¹ while practical systems have defects (e.g., step edged, grain boundaries, or phase domains) and are dynamic in nature^{53, 62}.

Fig. 5c reports the density of states (DOS) projected onto the molecular part of Ag-S(CH₂)₁₄X. All systems show a feature at ~1.5 eV (marked by * in Fig. 5c) that is due to Ag-S hybridization (see Section S8). Interestingly, we find that lower lying occupied states as well

as the lowest unoccupied state strongly shift in energy (on the order of 1-2 eV) with varying X (see arrows in Fig. 5c). These energy shifts clearly correlate with X functionalization and increase in magnitude along the halogen series, so that the X=I SAM shows pronounced new features close to the band edges when compared to the X=H or X=F SAM. Fig. 5d shows the DOS projected onto just the X-site in Ag-S(CH₂)₁₄X, which confirms that these new occupied and unoccupied states are due to the halogen functionalization. For both the occupied and unoccupied parts of the DOS, these halogen-derived states do partially overlap in energy with other features but are localized primarily at the tail of the SAM (see Section S8).

Finally, we determined ϵ_r as a function of X for the free-standing and hydrogen-terminated HS(CH₂)₁₄X SAMs using previously reported protocols^{44, 63} (see Table 1 and Section S8). In contrast to the above-discussed experimental results, we find that ϵ_r hardly changes with X functionalization in our DFT calculations. This result is expected from purely electrostatic reasoning and fully in line with previous work by various groups.^{42, 43, 44} Briefly, in these studies it has been shown from electrostatic and DFT calculations that varying the molecular polarizability of the SAM-forming molecules does not result in significant changes of ϵ_r in the densely-packed conjugated SAMs due to depolarization effects arising from the neighbouring molecular dipoles in the SAM^{42, 43, 44}. Therefore, the calculations show that tuning the molecular polarizability by changing X does not strongly impact the calculated ϵ_r of the HS(CH₂)₁₄X SAM.

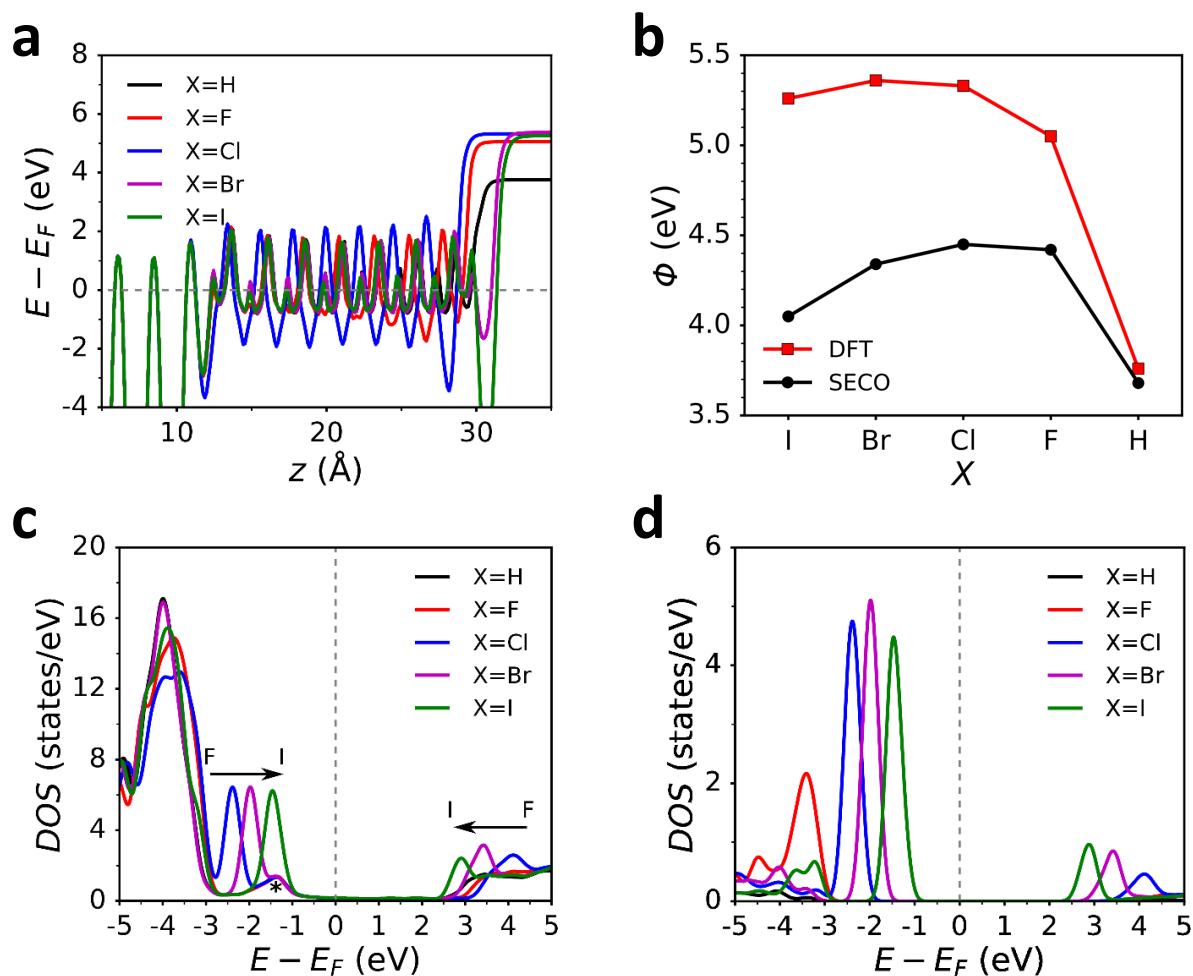


Figure 5. (a) DFT-calculated plane-averaged electrostatic potential of Ag(111)-S(CH₂)₁₄X where X = H, F, Cl, Br, or I, along the surface-normal coordinate. (b) Work function (Φ) of the SAMs, calculated from DFT (red squares) and measured experimentally (black dots). Density of states (DOS) projected onto the molecular backbone (c) and onto the X-site (d) of Ag(111)-S(CH₂)₁₄X. Note that X contributes very little to the band edges for X=H, F.

Discussion. Our theoretical finding that X functionalization does not dramatically alter ϵ_r of the SAM is in line with electrostatic considerations discussed in previous theoretical work.^{42, 43, 44} As pointed out by Kronik et al.,⁴³ a competition between suppression of in-plane polarization and enhancement of out-of-plane polarization occurs in SAMs. The suppression dominates for densely-packed SAMs and, thus, the substituent X should not affect the

calculated ϵ_r of the SAM in sharp contrast to our experimental findings⁵⁹. Our calculations as well as previous theoretical studies, however, only probe the intrinsic dielectric properties of the isolated highly organized SAM without contacts. The interaction between the SAM and the top electrode that is naturally present in the experimental determination of ϵ_r could affect the dielectric behaviour of the junction considerably, which would be consistent with the experimentally recorded trends for the R_C shown in Fig. 4a. Given the high electric fields on the order of GV/m and the polarizable nature of X, the substituents may be partially charged during charge transport (especially iodines are well-known to readily accommodate electrons)^{64,65}. We note that the physical significance and so predictive power of periodic DFT calculations previously reported by some of us⁴⁶ were limited by simulation artefacts of uncompensated dipoles in the unit cell which may have created a spurious correlation with measured ϵ_r values.

In the following, we discuss our results in the context of commonly used models to interpret charge transport through the $S(CH_2)_nX$ molecular junctions. The single-level Landauer model is frequently used to model the current flowing across molecular tunnel junctions.⁶⁶ The single-level Landauer model is also frequently used to model the current flowing across molecules junctions.⁶⁶ Here we modelled the current using the following expression:

$$I = N \frac{q}{h} \iint_{-\infty}^{\infty} dE dE' D_{E'}(E) G_{\delta E_{ME}}(E') \frac{\gamma_L \gamma_R}{\gamma_L + \gamma_R} [f_L(E) - f_R(E)], \quad (4)$$

where N is the number of molecules contributing to conduction, γ_L and γ_R are the tunneling rates between the molecule and the left and right electrodes (respectively), and $f_L(E)$ and $f_R(E)$ are the Fermi functions representing the electronic occupation of the left and right electrodes, respectively.⁶⁶ In addition, $D_{E'}(E)$ is the electronic density of states of the molecular level given by the following normalized Lorentzian function

$$D_{E'}(E) = \frac{\gamma/2\pi}{\left(E - \left(E' + \left(\eta - \frac{1}{2}\right)V\right)\right)^2 + (\gamma/2)^2}, \quad (5)$$

centred at energy $E' + \left(\eta - \frac{1}{2}\right)V$, where $\eta = V_R/(V_L + V_R)$ is the voltage division parameter accounting for the capacitive coupling with the left and right electrodes, and with a level width $\gamma = \gamma_L + \gamma_R$, where $\gamma_{L,R}$ are the electron tunneling rates between the molecule and the respective electrodes. A Gaussian function (with center δE_{ME} and width σ) represents the inherent dispersion (σ) of the molecular level energy (δE_{ME}) in an ensemble of molecules (rather than a single-molecule junction), as given by the following expression:

$$G_{\delta E_{ME}}(E') = A \exp\left(-\frac{(E' - \delta E_{ME})^2}{2\sigma^2}\right) \quad (6)$$

Good fittings to the data for all molecules (Fig. 6a and Table S11) are achieved for $T = 300$ K and the following common parameters are obtained across all molecules: $N = 50$, $\eta \in 0.48 \pm 0.02$, and $\sigma = 0.19$ eV. Figures 6b and 6c show the two parameters that vary across molecules: the energy δE_{ME} of the frontier orbital, which decreases on moving through the sequence H-F-Cl-Br-I (Fig. 6b), in agreement with the behaviour observed in spectroscopic data and determined by DFT calculations (although of lower values due to energy renormalization absent in our DFT calculations), and the overall tunnelling rate through the junction (i.e., molecule—electrode coupling strength), defined as $\Gamma = \frac{\gamma_L \gamma_R}{\gamma_L + \gamma_R}$, which increases exponentially along the halogen sequence (Fig. 6c) and accounts for the observed exponential increase of the current through the junctions.

Figure 6e shows a linear relationship between calculated $\sqrt{\delta E_{ME}}$ and measured β , which agrees with commonly used coherent tunnelling models^{2, 5, 21} including the Simmons model which also accounts for ϵ_r . However, the Simmons model also predicts a decrease of the tunnelling rates with increasing ϵ_r due to a reduction of the image charge effects in the

electrodes due to screening within the SAM.^{21, 67} This reduction of image charge in effect increases δE_{ME} and, consequently, β , but we observe the opposite trend. Using the same model, a reduction of the effective electron mass could also account for an increase in tunnelling rates, but it is not clear how the effective electron mass would change as a function of X with the essentially localized features derived from the highest occupied molecular orbital (HOMO) and lowest unoccupied molecular orbital (LUMO). Furthermore, Vilan argued that changes in the electron mass are equivalent to changes in the δE_{ME} within the Simmons model, which further complicates the interpretation of our findings within this framework.⁶⁸

The experimentally determined values of R_C have been related to Γ as $R_C \propto \Gamma^{-2}$,³⁴ *i.e.*, the coupling of the molecules with the electrode we have determined above (Fig. 6e). To test whether this holds for the SAMs studied here, Fig. 6e shows a double-log plot of R_C vs. $1/\Gamma^2$ indicating that our results can be explained, at least qualitatively, using this picture: changes in both δE_{ME} and Γ can lower β , in accordance with findings by others.^{10, 30, 31, 32, 33, 34, 35, 36, 37, 38, 39, 40} This approach, however, does not capture the observed changes in the dielectric response of the junctions directly, and, of course, it does not explicitly account for the local changes in the electrostatic potential profile induced by X observed in the DFT calculations; these effects are essentially compensated by the large change in Γ of 3 orders of magnitude.

An interesting finding was reported by Berlin and Ratner based on an alternative model to describe tunnelling across barriers with charge traps, with the finding that $\beta \propto 1/\sqrt{\epsilon_r}$.⁶⁹ In this framework, the distance dependence of the conductance is related to a thickness-dependent barrier akin to the one inherent to the Simmons model.^{68, 70} In their model, however, the barrier arises from the presence of localized charge traps along the path of charge migration leading to a non-linear potential drop between the macroscopic leads. Figure 6f shows the linear relation of the double-log plot of β vs. ϵ_r with a slope of -0.82 which is lower than the expected -0.5 from the model by Berlin *et al.*⁶⁹, but note that a change in the contact resistance or further

changes in the barrier shape are not taken into consideration in this model. In our experiments, however, the contact resistance changes and our DFT calculations show that the barrier shape at the SAM//top electrode interface is affected by X.

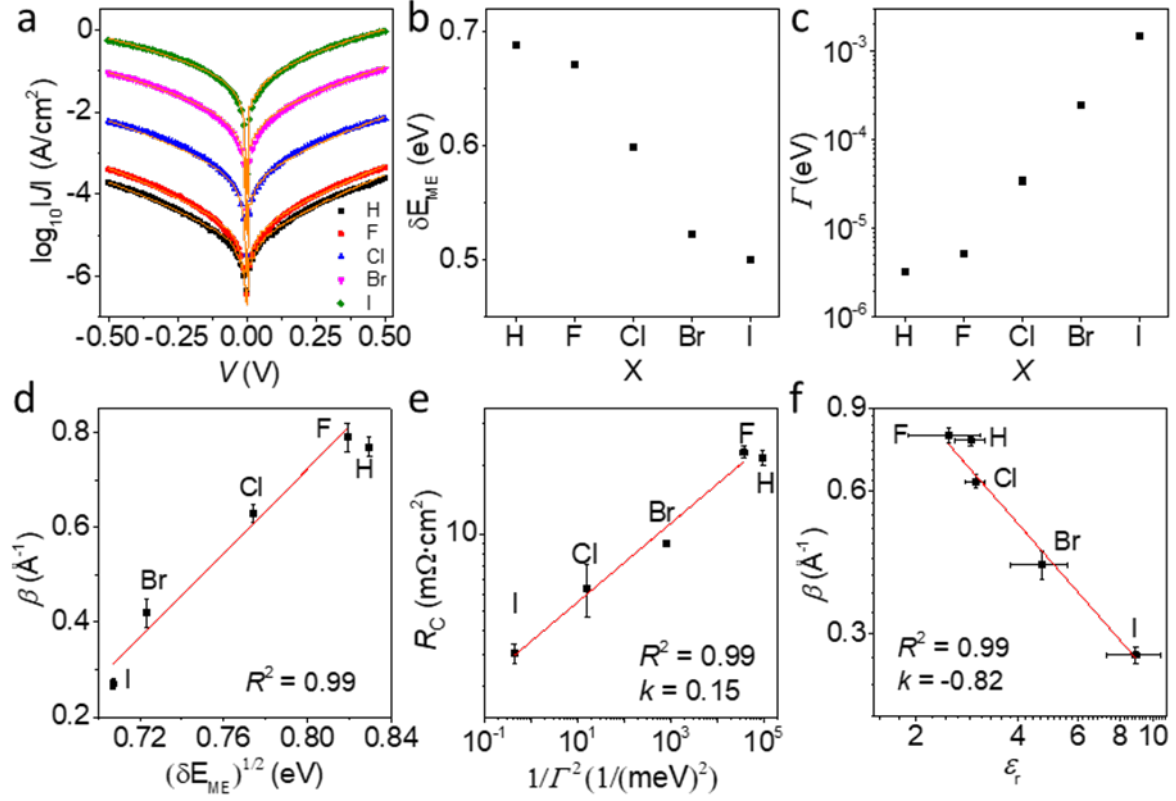


Figure 6. (a) The modelled current through the junctions using Landauer theory for a single level tunnel junction (orange solid lines are fits to the single level Landauer model, symbols represent experimental data). The values of δE_{ME} (b) and Γ (c) used for modelling the current through the junctions. (d) β vs. $\sqrt{\delta E_{ME}}$ with a linear fit (red line). (e) Double-log plot of R_C vs. $1/\Gamma^2$ where the red line is a power-law fit with a slope of 0.15 and $R^2 = 0.99$. (f) Double-log plot of β vs. ϵ_r where the red line is a fit with a slope of -0.82 and $R^2 = 0.99$.

Conclusions

This work shows that substitution of a single highly polarizable atom can have a pronounced effect on the energy level alignment, charge transport rate and dielectric response

of molecular junctions. We were able to tune the tunnelling decay coefficient β over a wide range from 0.25 \AA^{-1} to 0.75 \AA^{-1} across saturated alkyl chains by changing one atom per molecule inside large-area ($\sim 350 \text{ \mu m}^2$)⁵³ junctions. Combining experiment with DFT and Landauer charge transport models, we established three factors that contribute to the dramatic change in β of these aliphatic halogenated junctions with varying X and associated increase in α and ϵ_r : 1) The HOMO-LUMO gap^{5,46} and associated δE_{ME} is reduced which lowers β , 2) the shape of the tunnelling barrier is modified at the SAM-top electrode interface, resulting in larger potential drops at this interface, and 3) the electronic coupling Γ of the molecular orbitals with the electrodes increases (potentially because of an increase in the van der Waals interactions along the halogen series).

In a broad context of widely used charge tunnelling mechanisms, our findings point out their limitations highlighting the need for improved models that take dielectric (or collective) effects of the junctions into consideration. Specifically, the popular Simmons model predicts that image charge effects in the electrodes are reduced with increasing ϵ_r , resulting in lowering of the tunnelling rates⁶⁸, which is in sharp contrast to what we find. Superexchange models^{22,23,24} also fail to explain our observations, since the coupling between the molecular repeat unit (*i.e.*, the CH_2 units) was not changed here. Conversely, the Landauer model⁶⁶ could explain our results at least qualitatively, but not quantitatively. This is because it does not treat electrostatic effects in the junctions explicitly and self-consistently which resulted in our case in a very broad range of 3 orders of magnitude in the values of Γ even though the contact resistance only changed by a factor of 5 in our experiments. Interestingly, a mechanism proposed by Berlin and Ratner⁶⁹ that is based on charge traps provides a hypothesis for how the value of β could decrease with increasing ϵ_r . Although the physical interpretation differs as the tunnelling behaviour is explained in terms of charge traps rather than the electrostatic response of the SAM inside the junction, this line of thought stimulates further theoretical and experimental

testing of the presence of “impurities” – here in the form of polarizable atoms – as charge carriers that move across the energy band profiles. Although our findings suggest a correlation between β and ϵ_r , the increase of ϵ_r as function of X could not be reproduced in our DFT calculations, which may be because the calculations do not take the SAM–metal interface into consideration and, perhaps other factors are important such as (partial) charging of highly polarizable molecules during charge transport inside the junctions. To summarize, our work proposes an effective way of tuning the tunnelling rates across molecular junctions without chemically altering the backbone of the molecules and highlights the importance of understanding dielectric effects in these junctions. We hope that our findings will stimulate further experimental and theoretical investigations towards establishing improved transport mechanisms for junctions in their *in situ* physicochemical and electronic states inside working devices.

Data availability

The data that support the findings of this study are available from the corresponding author upon reasonable request.

References

1. Shah, A. et al. Electron transfer in peptides. *Chem. Soc. Rev.* **44**, 1015-1027 (2015).
2. Vilan, A., Aswal, D. & Cahen, D. Large-area, ensemble molecular electronics: motivation and challenges. *Chem. Rev.* **117**, 4248-4286 (2017).
3. Jortner, J., Nitzan, A. & Ratner, M. A. Foundations of Molecular Electronics – Charge Transport in Molecular Conduction Junctions. In *Introducing Molecular Electronics* (eds Cuniberti, G., Richter, K. & Fagas, G.) 13-54 (Springer, 2005).
4. Jia, C. & Guo, X. Molecule–electrode interfaces in molecular electronic devices. *Chem. Soc. Rev.* **42**, 5642-5660 (2013).
5. Metzger, R. M. Unimolecular electronics. *Chem. Rev.* **115**, 5056-5115 (2015).

6. Jeong, H., Kim, D., Xiang, D. & Lee, T. High-yield functional molecular electronic devices. *ACS Nano* **11**, 6511-6548 (2017).
7. Hylke, B. A. & Bert de, B. Electrical conduction through single molecules and self-assembled monolayers. *J. Phys.: Condens. Matter* **20**, 013001 (2008).
8. Nitzan, A. Electron transmission through molecules and molecular interfaces. *Annu. Rev. Phys. Chem.* **52**, 681-750 (2001).
9. Xie, Z., Bâldea, I. & Frisbie, C. D. Determination of energy-level alignment in molecular tunnel junctions by transport and spectroscopy: self-consistency for the case of oligophenylene thiols and dithiols on Ag, Au, and Pt electrodes. *J. Am. Chem. Soc.* **141**, 3670-3681 (2019).
10. Choi, S. H., Kim, B. & Frisbie, C. D. Electrical resistance of long conjugated molecular wires. *Science* **320**, 1482 (2008).
11. Kumar, K. S., Neoh, E. H. L., Vilan, A. & Nijhuis, C. A. Protective layers based on carbon paint to yield high-quality large-area molecular junctions with low contact resistance. *J. Am. Chem. Soc.* **142**, 3513-3524 (2020).
12. Simeone, F. C. et al. Defining the value of injection current and effective electrical contact area for EGaIn-based molecular tunneling junctions. *J. Am. Chem. Soc.* **135**, 18131-18144 (2013).
13. Wold, D. J., Haag, R., Rampi, M. A. & Frisbie, C. D. Distance dependence of electron tunneling through self-assembled monolayers measured by conducting probe atomic force microscopy: unsaturated versus saturated molecular junctions. *J. Phys. Chem. B* **106**, 2813-2816 (2002).
14. Karuppanan, S. K., Pasula, R. R., Lim, S. & Nijhuis, C. A. Long-range tunneling processes across ferritin-based junctions. *Adv. Mater.* **28**, 1824-1830 (2016).
15. Christopher, D. B. et al. Protein bioelectronics: a review of what we do and do not know. *Rep. Prog. Phys.* **81**, 026601 (2018).
16. Baghbanzadeh, M. et al. Charge tunneling along short oligoglycine chains. *Angew. Chem. Int. Ed.* **54**, 14743-14747 (2015).
17. Baghbanzadeh, M. et al. Anomalously rapid tunneling: charge transport across self-assembled monolayers of oligo(ethylene glycol). *J. Am. Chem. Soc.* **139**, 7624-7631 (2017).
18. Su, T. A., Li, H., Steigerwald, M. L., Venkataraman, L., & Nuckolls, C. Stereoelectronic switching in single-molecule junctions. *Nat. Chem.* **7**, 215-220 (2015).
19. Merces, L., de Oliveira, R. F., de Camargo, D. H. S. & Bufon, C. C. B. Long-range coherent tunneling in physisorbed molecular ensembles. *J. Phys. Chem. C* **121**, 16673-16681 (2017).
20. Yan, H. et al. Activationless charge transport across 4.5 to 22 nm in molecular electronic junctions. *Proc. Natl. Acad. Sci. USA* **110**, 5326-5330 (2013).

21. Simmons, J. G. Generalized formula for the electric tunnel effect between similar electrodes separated by a thin insulating film. *J. Appl. Phys.* **34**, 1793-1803 (1963).
22. Naleway, C. A., Curtiss, L. A. & Miller, J. R. Superexchange-pathway model for long-distance electronic couplings. *J. Phys. Chem.* **95**, 8434-8437 (1991).
23. McConnell, H. M. Intramolecular charge transfer in aromatic free radicals. *J. Chem. Phys.* **35**, 508-515 (1961).
24. Todd, M. D., Nitzan, A. & Ratner, M. A. Electron transfer via superexchange: a time-dependent approach. *J. Phys. Chem.* **97**, 29-33 (1993).
25. Juhaniwicz, J. & Sek, S. Peptide molecular junctions: Distance dependent electron transmission through oligoprolines. *Bioelectrochem.* **87**, 21-27 (2012).
26. Beratan, D. N. et al. Charge transfer in dynamical biosystems, or the treachery of (static) images. *Acc. Chem. Res.* **48**, 474-481 (2015).
27. Zhang, Y., Liu, C., Balaeff, A., Skourtis, S. S. & Beratan, D. N. Biological charge transfer via flickering resonance. *Proc. Natl. Acad. Sci. USA.* **111**, 10049-10054 (2014).
28. Berlin, Y. A., Kurnikov, I. V., Beratan, D., Ratner, M. A. & Burin, A. L. DNA Electron Transfer Processes: Some Theoretical Notions. In *Long-Range Charge Transfer in DNA II* (eds Schuster, G. B.) 1-36 (Springer, 2004).
29. Amdursky, N. et al. Electronic transport via proteins. *Adv. Mater.* **26**, 7142-7161 (2014).
30. Sangeeth, C. S. S. et al. Comparison of DC and AC transport in 1.5–7.5 nm oligophenylene imine molecular wires across two junction platforms: eutectic Ga–In versus conducting probe atomic force microscope junctions. *J. Am. Chem. Soc.* **138**, 7305-7314 (2016).
31. Nguyen, Q. V. et al. Highly efficient long-range electron transport in a viologen-based molecular junction. *J. Am. Chem. Soc.* **140**, 10131-10134 (2018).
32. Choi, S.H. et al. Transition from tunneling to hopping transport in long, conjugated oligo-imine wires connected to metals. *J. Am. Chem. Soc.* **132**, 4358-4368 (2010).
33. Sepunaru, L. et al. Electronic transport via homopeptides: the role of side chains and secondary structure. *J. Am. Chem. Soc.* **137**, 9617-9626 (2015).
34. Xie, Z., Bâldea, I., Smith, C. E., Wu, Y. & Frisbie, C. D. Experimental and theoretical analysis of nanotransport in oligophenylene dithiol junctions as a function of molecular length and contact work function. *ACS Nano* **9**, 8022-8036 (2015).
35. Gunasekaran, S. et al. Near length-independent conductance in polymethine molecular wires. *Nano Lett.* **18**, 6387-6391 (2018).
36. Sedghi, G. et al. Long-range electron tunnelling in oligo-porphyrin molecular wires. *Nat. Nanotechnol.* **6**, 517-523 (2011).

37. Leary, E. et al. Bias-driven conductance increase with length in porphyrin tapes. *J. Am. Chem. Soc.* **140**, 12877-12883 (2018).
38. Zhang, Y. et al. Tunneling probability increases with distance in junctions comprising self-assembled monolayers of oligothiophenes. *J. Am. Chem. Soc.* **140**, 15048-15055 (2018).
39. Algethami, N., Sadeghi, H., Sangtarash, S. & Lambert, C. J. The conductance of porphyrin-based molecular nanowires increases with length. *Nano Lett.* **18**, 4482-4486 (2018).
40. Stuyver, T., Zeng, T., Tsuji, Y., Geerlings, P. & De Proft, F. Diradical character as a guiding principle for the insightful design of molecular nanowires with an increasing conductance with length. *Nano Lett.* **18**, 7298-7304 (2018).
41. Sangeeth, C. S. S., Wan, A. & Nijhuis, C. A. Equivalent circuits of a self-assembled monolayer-based tunnel junction determined by impedance spectroscopy. *J. Am. Chem. Soc.* **136**, 11134-11144 (2014).
42. Van Dyck, C., Marks, T. J. & Ratner, M. A. Chain length dependence of the dielectric constant and polarizability in conjugated organic thin films. *ACS Nano* **11**, 5970-5981 (2017).
43. Natan, A., Kuritz, N. & Kronik, L. Polarizability, susceptibility, and dielectric constant of nanometer-scale molecular films: a microscopic view. *Adv. Funct. Mater.* **20**, 2077-2084 (2010).
44. Romaner, L., Heimel, G., Ambrosch-Draxl, C. & Zojer, E. The dielectric constant of self-assembled monolayers. *Adv. Funct. Mater.* **18**, 3999-4006 (2008).
45. Obersteiner, V. et al. Electrostatic design of 3d covalent organic networks. *Adv. Mater.* **29**, 1700888 (2017).
46. Wang, D. et al. Tuning the tunneling rate and dielectric response of SAM-based junctions via a single polarizable atom. *Adv. Mater.* **27**, 6689-6695 (2015).
47. Haj-Yahia, A-E. et al. Substituent variation drives metal/monolayer/semiconductor junctions from strongly rectifying to ohmic behavior. *Adv. Mater.* **25**, 702-706 (2013).
48. Mazinani, S. K. S. et al. Polarizability as a molecular descriptor for conductance in organic molecular circuits. *J. Phys. Chem. C* **120**, 26054-26060 (2016).
49. Baghbanzadeh, M., Pieters, P. F., Yuan, L., Collison, D. & Whitesides, G. M. The rate of charge tunneling in EGaIn junctions is not sensitive to halogen substituents at the self-assembled monolayer//Ga₂O₃ interface. *ACS Nano* **12**, 10221-10230 (2018).
50. Stone, A. J. The theory of intermolecular forces, 2nd ed. *Oxford University Press* (2013).
51. Lampion, Z. A. et al. Fluorinated benzalkylsilane molecular rectifiers. *Sci. Rep.* **6**, 38092 (2016).
52. Nerngchamnong, N. et al. The role of van der Waals forces in the performance of molecular diodes. *Nat. Nanotechnol.* **8**, 113-118 (2013).

53. Chen, X., Hu, H., Trasobares, J. & Nijhuis, C. A. Rectification ratio and tunneling decay coefficient depend on the contact geometry revealed by in situ imaging of the formation of EGaIn junctions. *ACS Appl. Mater. Inter.* **11**, 21018-21029 (2019).
54. Wang, W., Lee, T. & Reed, M. A. Mechanism of electron conduction in self-assembled alkanethiol monolayer devices. *Phys. Rev. B* **68**, 035416 (2003).
55. Jiang, L., Sangeeth, C. S. S. & Nijhuis, C. A. The origin of the odd–even effect in the tunneling rates across EGaIn junctions with self-assembled monolayers (SAMs) of n-alkanethiolates. *J. Am. Chem. Soc.* **137**, 10659-10667 (2015).
56. Ashcroft, N. W. & Mermin, N. D. *Solid State Physics* (Holt, Rinehart and Winston, 1976).
57. Kresse, G. & Furthmüller, J. Efficient iterative schemes for ab initio total-energy calculations using a plane-wave basis set. *Phys. Rev. B* **54**, 11169-11186 (1996).
58. Lee, H. J., Jamison, A. C. & Lee, T. R. Surface Dipoles: a growing body of evidence supports their impact and importance. *Acc. Chem. Res.* **48**, 3007-3015 (2015).
59. Chen, X. et al. Interplay of collective electrostatic effects and level alignment dictates the tunneling rates across halogenated aromatic monolayer junctions. *J. Phys. Chem. Lett.* **10**, 4142-4147 (2019).
60. Asyuda, A., Wan, X. & Zharnikov, M. Binary aromatic self-assembled monolayers: electrostatic properties and charge tunneling rates across the molecular framework. *Phys. Chem. Chem. Phys.* **22**, 10957-10967 (2020).
61. Abu-Husein, T. et al. The effects of embedded dipoles in aromatic self-assembled monolayers. *Adv. Funct. Mater.* **25**, 3943-3957 (2015).
62. Jiang, L., Sangeeth, C. S. S., Yuan, L., Thompson, D. & Nijhuis, C. A. One-nanometer thin monolayers remove the deleterious effect of substrate defects in molecular tunnel junctions. *Nano Lett.* **15**, 6643-6649 (2015).
63. Heitzer, H. M., Marks, T. J. & Ratner, M. A. First-principles calculation of dielectric response in molecule-based materials. *J. Am. Chem. Soc.* **135**, 9753-9759 (2013).
64. Rozhkov, I. N., Raevsky, A. M., Gushchin, S. I., Ignatova, J. L. & Semin, G. K. Evaluation of charge changes on chlorine, bromine and iodine atoms in perfluoroalkyl halogenides based on nuclear quadrupole resonance data. *J. Fluor. Chem.* **58**, 234-234 (1992).
65. Probst, A., Raab, K., Ulm, K. & von Werner, K. Synthesis and chemistry of perfluoro-2-iodo-2-methyl-alkanes. *J. Fluor. Chem.* **37**, 223-245 (1987).
66. Simmons, J. G. Electric tunnel effect between dissimilar electrodes separated by a thin insulating film. *J. Appl. Phys.* **34**, 2581-2590 (1963).

67. Vilan, A. Analyzing molecular current-voltage characteristics with the simmons tunneling model: scaling and linearization. *J. Phys. Chem. C* **111**, 4431-4444 (2007).
68. Garrigues, A. R. et al. A single-level tunnel model to account for electrical transport through single molecule- and self-assembled monolayer-based junctions. *Sci. Rep.* **6**, 26517 (2016).
69. Berlin, Y. A. & Ratner, M. A. Conduction of metal–thin organic film–metal junctions at low bias. *J. Phys. Chem. C* **122**, 7557-7563 (2018).
70. Karuppanan, S. K., Hu, H., Troadec, C., Vilan, A. & Nijhuis, C. A. Ultrasoft and photoresist-free micropore-based EGaIn molecular junctions: fabrication and how roughness determines voltage response. *Adv. Funct. Mater.* **29**, 1904452 (2019).

Acknowledgements

We acknowledge fruitful discussions with Ayelet Vilan (Weizmann Institute of Science) and Gemma Solomon (University of Copenhagen). Funding by the Ministry of Education (MOE) for supporting this research under award No. MOE2019-T2-1-137 is acknowledged. Prime Minister's Office, Singapore under its Medium sized centre program is also acknowledged for supporting this research. The authors would furthermore like to acknowledge the Singapore Synchrotron Light Source (SSLS) for providing the facilities at the Surface, Interface and Nanostructure Science (SINS) beam line under NUS core support C-380-003-003-001. The Laboratory is a National Research Infrastructure under the National Research Foundation Singapore. We moreover acknowledge funding from the Alexander von Humboldt Foundation within the framework of the Sofja Kovalevskaja Award, endowed by the German Federal Ministry of and Research, and the Technical University of Munich - Institute for Advanced Study, funded by the German Excellence Initiative and the European Union Seventh Framework Programme under Grant Agreement No. 291763. DT thanks Science Foundation Ireland (SFI) for support (awards Grant Numbers 15/CDA/3491 and 12/RC/2275_P2) and for computing resources at the SFI/Higher Education Authority Irish Centre for High-End Computing (ICHEC). Finally, we also acknowledge support from the U.S. National Science Foundation (Grant no. ECCS#1916874).

Author information

Affiliations

Department of Chemistry, National University of Singapore, 3 Science Drive 3, Singapore 117543, Singapore

Xiaoping Chen, Christian A. Nijhuis

Centre for Advanced 2D Materials and Graphene Research Centre, National University of Singapore, 6 Science Drive 2, Singapore 117546, Singapore

Xiaoping Chen, Christian A. Nijhuis

Department of Physics, Technical University of Munich, 85748 Garching, Germany

Bernhard Kretz, David A. Egger

Department of Physics, University of Central Florida, Orlando, Florida 32816 - USA

Francis Adoah, Cameron Nickle, Enrique del Barco

Singapore Synchrotron Light Source, National University of Singapore, 5 Research Link, Singapore 117603, Singapore

Xiao Chi, Xiaojiang Yu

Department of Physics, Bernal Institute, University of Limerick, V94 T9PX, Ireland

Damien Thompson

Contributions

X. C., D. A. E.; and C. A. N. conceived and designed the project. X. C. synthesized the compounds, performed electrical characterizations, and associated data analysis; B. K. and D. A. E. performed the DFT calculations; F. A., C. N.; and E. B. performed the Landauer model analysis; X. C. and X. Y. conducted the XPS and UPS measurements; D. T. conducted the molecular dynamics; all the authors discussed the results and prepared the manuscript.

Corresponding authors

Correspondence to Christian A. Nijhuis or David A. Egger

Competing interests

The authors declare no competing financial interest.

Additional information

Peer review information Nature Communications thanks the anonymous reviewers for their contributions to the peer review of this work. Peer review reports are available.

Publisher's note Springer Nature remains neutral with regard to jurisdictional claims in published maps and institutional affiliations.

Supplementary information

Supporting Information contains materials and methods used in the paper, the synthesis of the molecules, the surface characterization of the SAMs on Ag, the electrical $J(V)$ and impedance results, the details of DFT calculations (PDF).

Figures

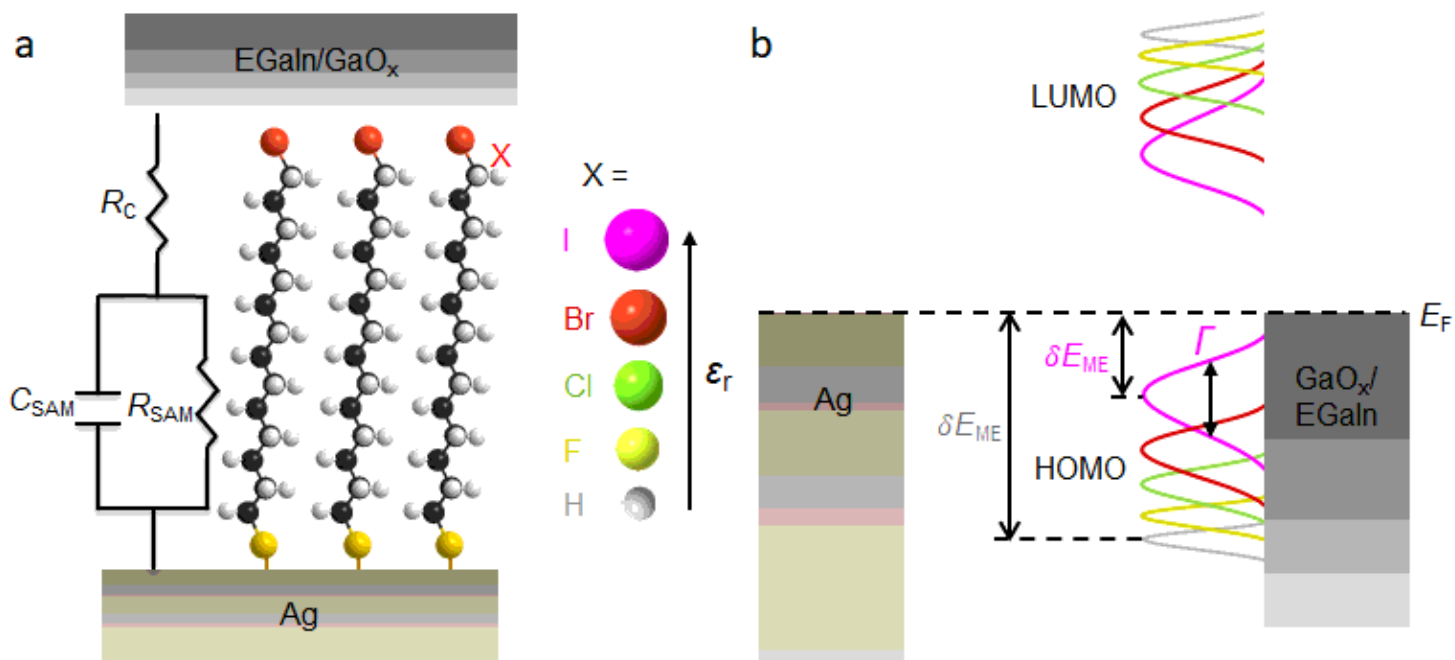


Figure 1

(a) Schematic illustration of the Ag-S(CH₂)_nX//GaO_x/EGaIn junction (shown for n = 14) together with the equivalent circuit diagram. In this work we investigated junctions with n = 10, 12, 14, 16, or 18, and X = H, F, Cl, Br, or I. (b) Energy level diagram of the junction showing how Γ and δE_{ME} change with X.

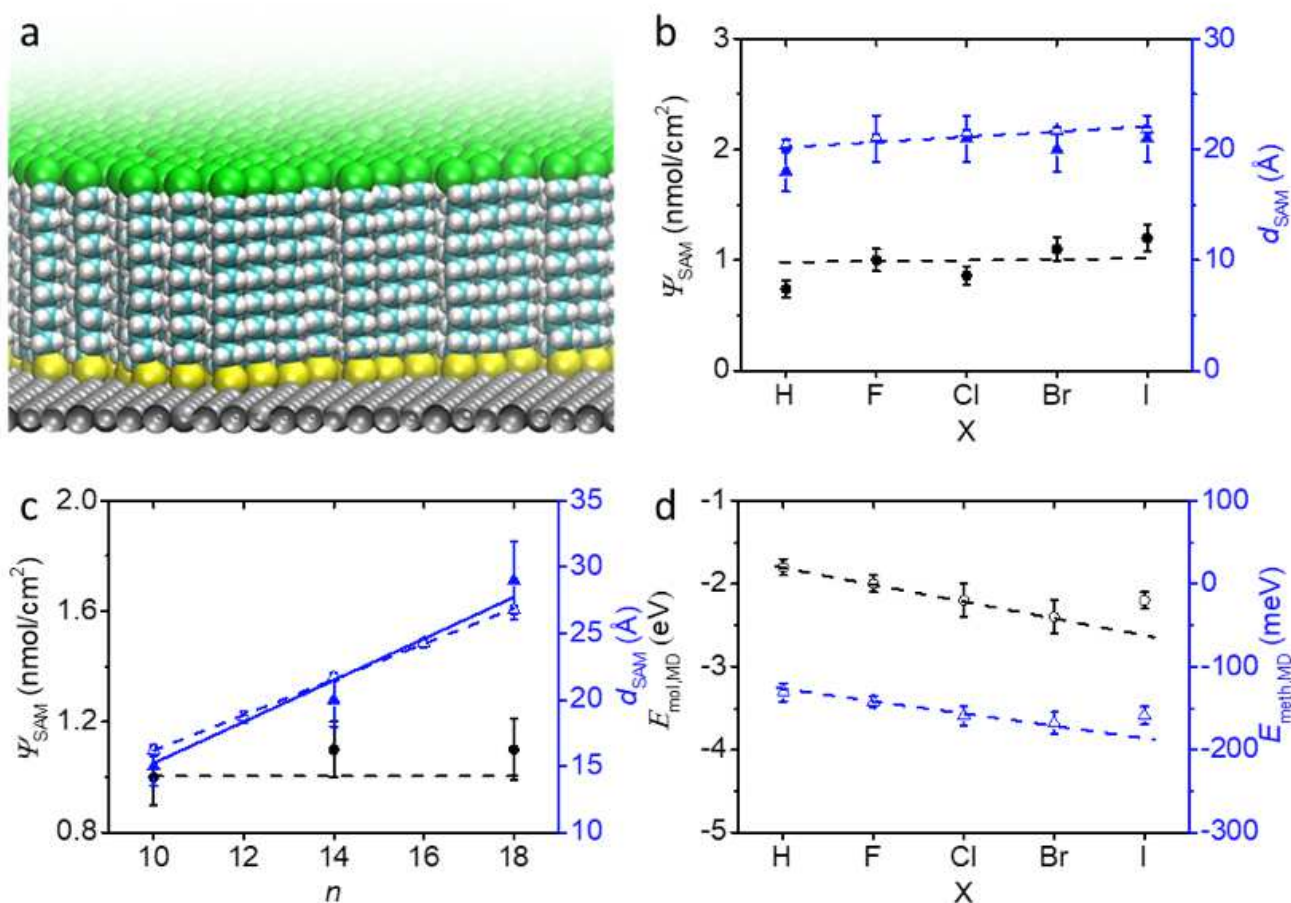


Figure 2

(a) Representative slice-through of a large-area Ag-S(CH₂)₁₄I SAM structure calculated by MD computer simulations. (b) Ψ_{SAM} of Ag-S(CH₂)₁₄X SAMs as a function of X determined with ARXPS (filled circles) and d_{SAM} determined with ARXPS (filled triangles) and MD (empty triangles). (c) Ψ_{SAM} of Ag-S(CH₂)_nBr SAMs as a function of n determined with ARXPS (filled circles) and d_{SAM} determined with ARXPS (filled triangles) and MD (open triangles). The solid and dashed blue lines are linear fits to the experimental and MD data with R² of 0.94 and 0.99, respectively. The horizontal dashed line in panels b and c indicates the Ψ_{SAM} used in the MD calculations. (d) Computed MD packing energy per molecule $E_{\text{mol,MD}}$ and per methylene -CH₂- unit $E_{\text{meth,MD}}$ of Ag-S(CH₂)₁₄X SAMs as a function of X. Dashed lines are guides to the eye. The errors on the XPS data represent instrumental and fitting errors of 10% in total (see Section S4). The error bars in the MD data represent the standard deviations in the time- and molecule-averages calculated across 500 snapshots taken during the final 50 ns of 100 ns of room temperature MD of 128-molecule Ag-S(CH₂)₁₄X SAMs with the average experimental coverage of 1 nmol/cm² on Ag(111).

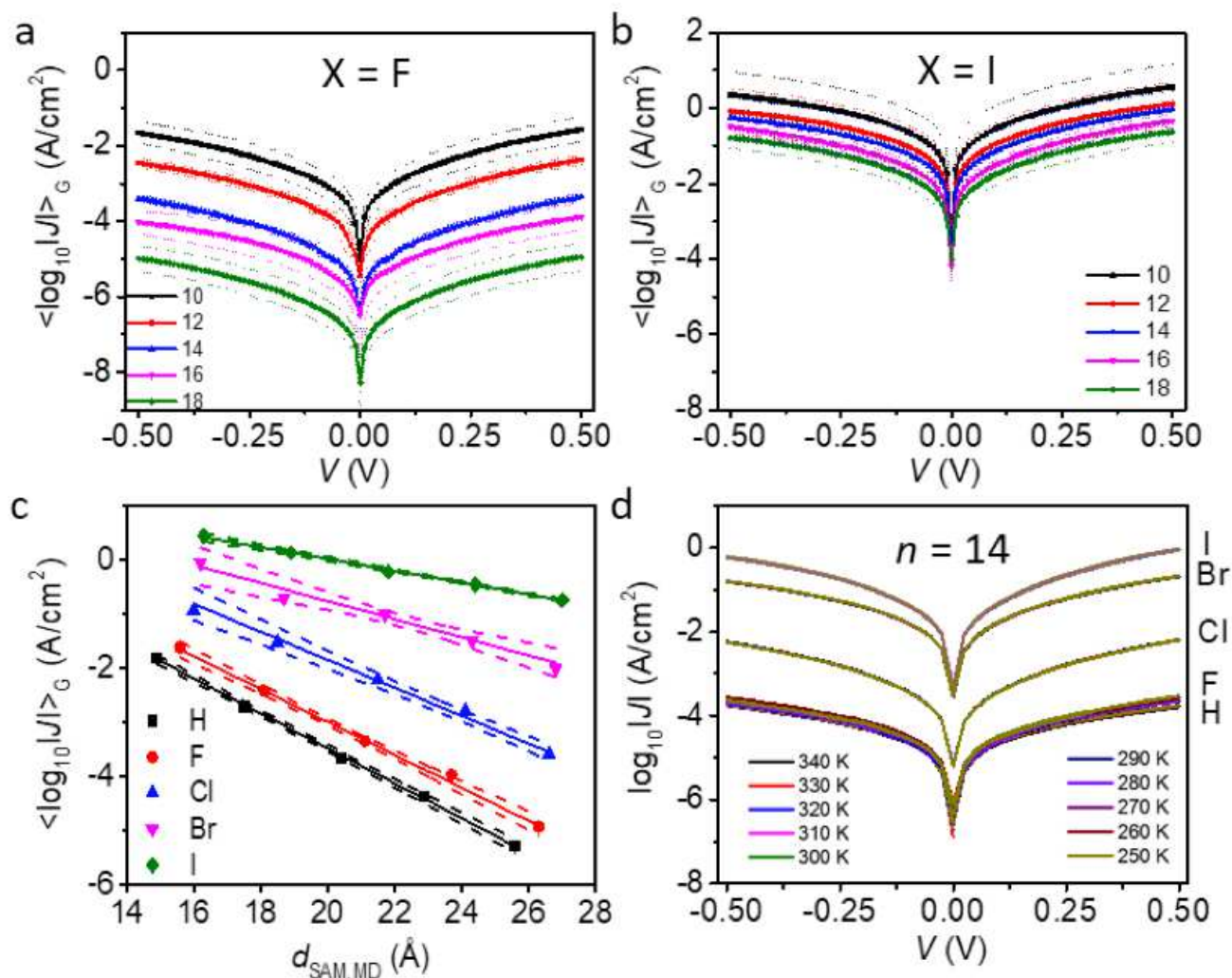


Figure 3

$\langle \log_{10}|J| \rangle_G$ vs. V obtained from Ag-S(CH₂)_nX//GaO_x/EGaIn junctions with $X = F$ (a) or I (b) and $n = 10$ (solid black line), 12 (solid red line), 14 (solid blue line), 16 (solid pink line), and 18 (solid green line). The dashed-line error bars represent the Gaussian log-standard deviation, $\sigma_{\log,G}$. (c) Decay plots of $\langle \log_{10}|J| \rangle_G$ at -0.5 V against $d_{\text{SAM,MD}}$ with $X = H$ (black square), F (red circle), Cl (blue triangle), Br (pink inverted triangle), or I (green diamond). The solid lines are fits to Eq. 1. The dashed lines represent the 95% confidence bands. (d) Plots of $\log_{10}|J|$ vs. V as a function of T ($T = 250 - 340$ K) recorded from Ag-S(CH₂)₁₄X//GaO_x/EGaIn junctions.

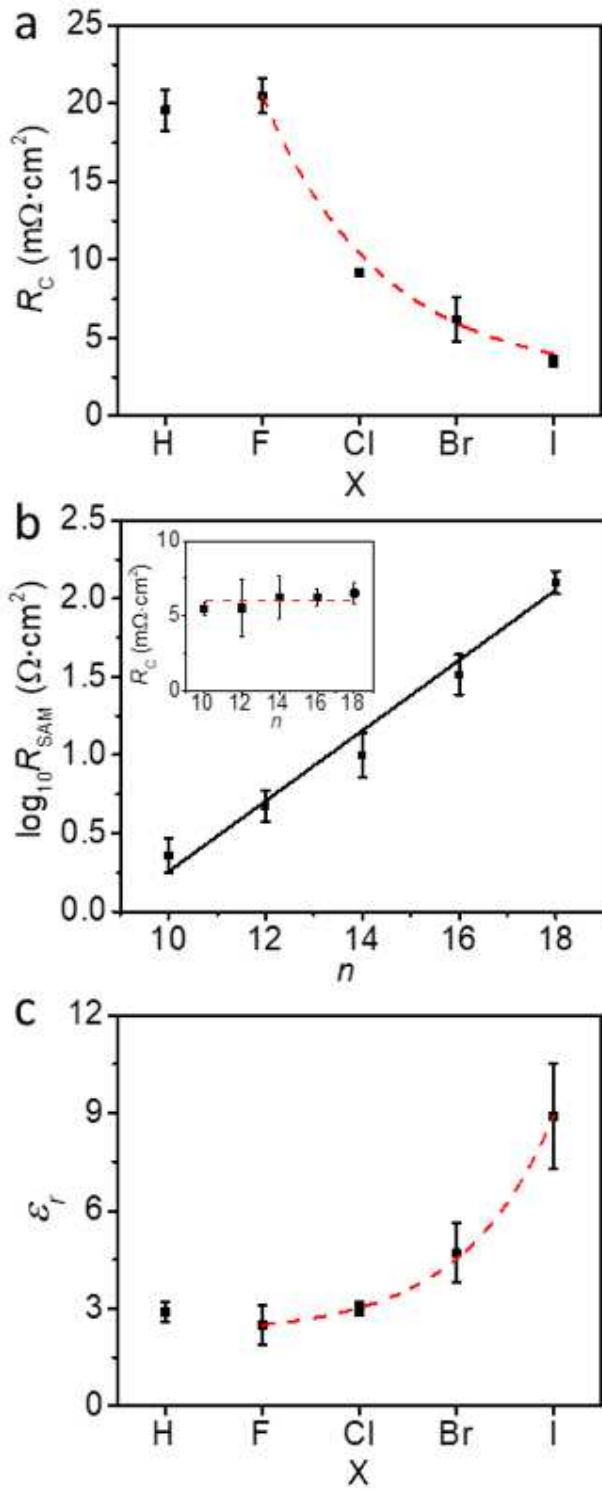


Figure 4

(a) R_C vs. X for Ag-S(CH₂)₁₄X//GaOx/EGaIn junctions at 0 V. (b) $\log_{10} R_{SAM}$ and R_C (inset) vs. n for Ag-S(CH₂)_nBr//GaOx/EGaIn junctions at 0 V. The solid black line represents a fit to Eq. 2. (c) ϵ_r vs. X for Ag-S(CH₂)₁₄X//GaOx/EGaIn junctions at 0 V. The error bars are the standard deviations of three independent measurements. Dashed lines are visual guides.

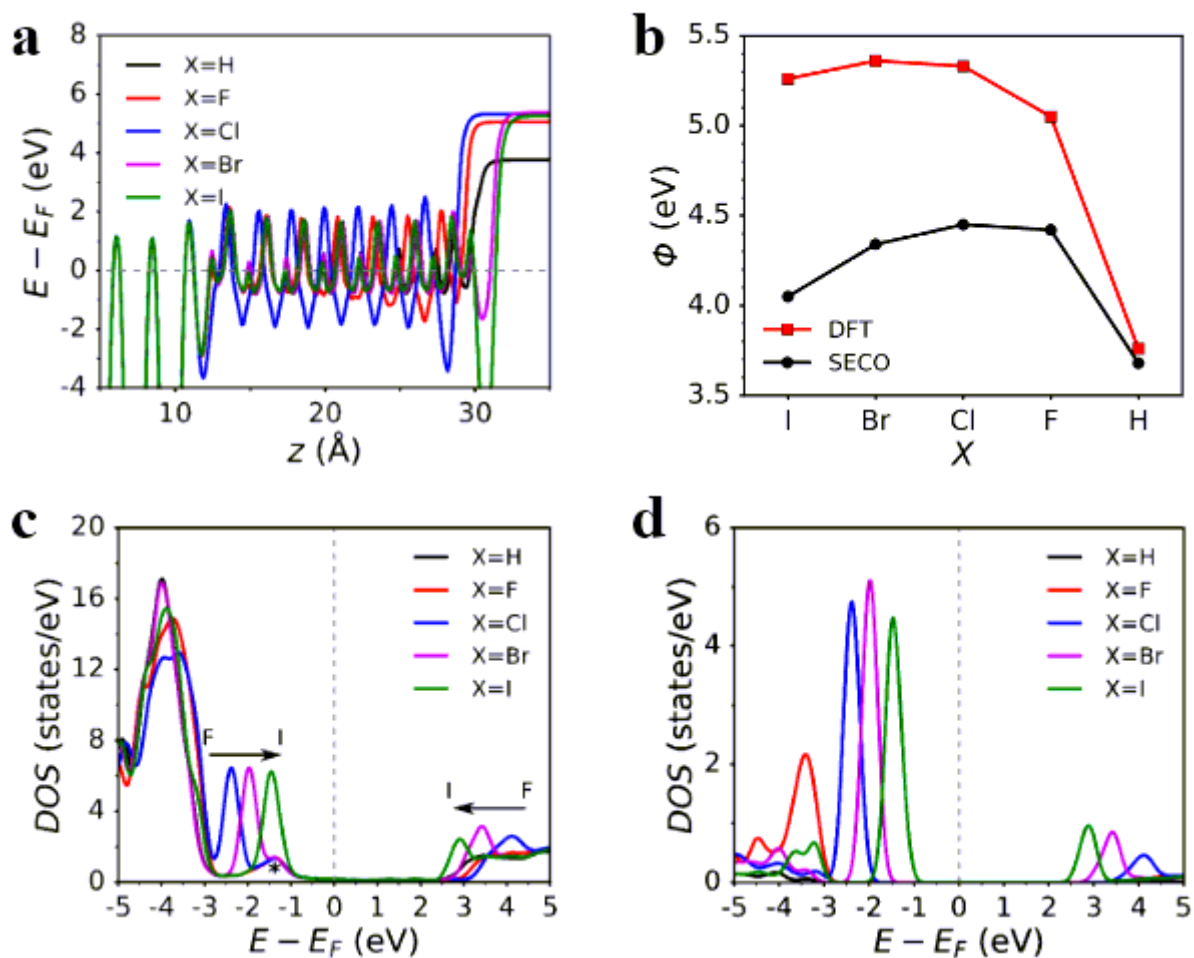


Figure 5

(a) DFT-calculated plane-averaged electrostatic potential of Ag(111)-S(CH₂)₁₄X where X = H, F, Cl, Br, or I, along the surface-normal coordinate. (b) Work function (Φ) of the SAMs, calculated from DFT (red squares) and measured experimentally (black dots). Density of states (DOS) projected onto the molecular backbone (c) and onto the X-site (d) of Ag(111)-S(CH₂)₁₄X. Note that X contributes very little to the band edges for X=H, F.

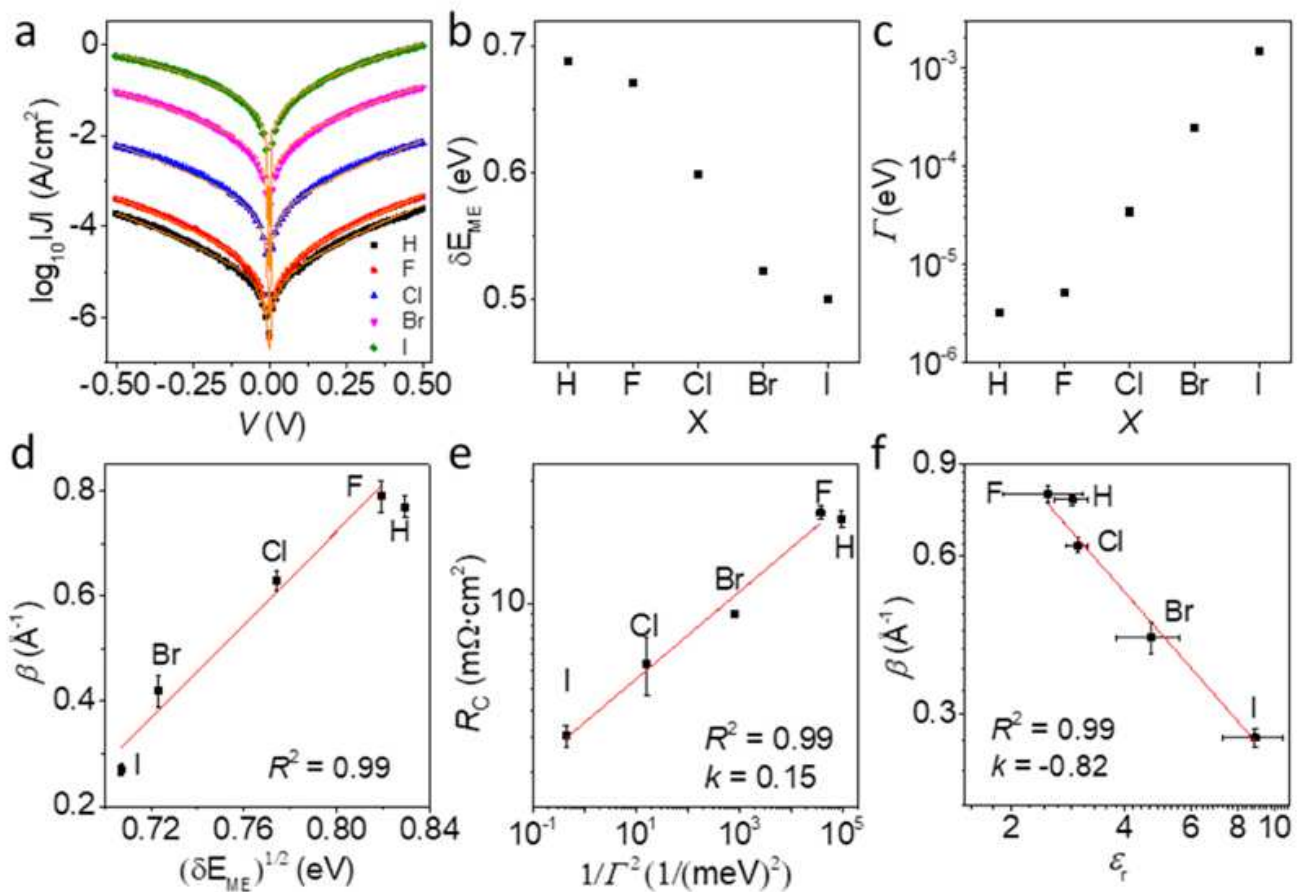


Figure 6

(a) The modelled current through the junctions using Landauer theory for a single level tunnel junction (orange solid lines are fits to the single level Landauer model, symbols represent experimental data). The values of δE_{ME} (b) and Γ (c) used for modelling the current through the junctions. (d) β vs. $\sqrt{(\delta E_{ME})}$ with a linear fit (red line). (e) Double-log plot of R_C vs. $1/\Gamma^2$ where the red line is a power-law fit with a slope of 0.15 and $R^2 = 0.99$. (f) Double-log plot of β vs. ϵ_r where the red line is a fit with a slope of -0.82 and $R^2 = 0.99$.

Supplementary Files

This is a list of supplementary files associated with this preprint. Click to download.

- [Supplementaryinformation.docx](#)